Bull. Mater. Sci. _####################_
https://doi.org/10.1007/s12034-026-03752-y

Dual-mode operation of solution-combustion-derived nonstoichiometric $PrNi_{0.5}Co_{0.5}O_{3-\delta}$ oxygen electrode for direct 8YSZ based RSOFCs

SREELAKSHMI AMBILI[1,2], PACKIARAJ RAJAGOPAL[3], NAEEMAKHTAR MOMIN[4], VISWABASKARAN VISWANATHAN[5], SENTHIL KUMAR SELVARAJ[1,2,*] and ARUNA SINGANAHALLI THIPPAREDDY[1,2,*]

[1] Surface Engineering Division, CSIR -National Aerospace Laboratories, Bengaluru 560017, India
[2] Academy of Scientific and Innovative Research (AcSIR), Ghaziabad 201002, India
[3] Institute of Physical and Technical Sciences, L.N. Gumilyov Eurasian National University, Astana 010008, Kazakhstan
[4] Department of Chemistry, Sangolli Rayanna First Grade Constituent College, Belagavi 590017, India
[5] VB Ceramics Consultants, Nehru Nagar Industrial Estate, Kottivakkam, Chennai 600041, India
*Author for correspondence (ssenthil@nal.res.in; aruna_reddy@nal.res.in)

MS received 9 March 2026; accepted 27 July 2026

Abstract. Phase-pure orthorhombic $PrNi_{0.5}Co_{0.5}O_{3-\delta}$ (PNCO), a triple-conducting perovskite oxygen electrode material considered a promising alternative to conventional oxygen electrodes for reversible solid oxide fuel cells (RSOFCs), was synthesized using the solution combustion method. The synthesized powder exhibited a bimodal particle-size distribution with an average agglomerated particle size of ~0.24 μm. Iodometric titration revealed an oxygen non-stoichiometry (δ) of 0.09. PNCO exhibited an electrical conductivity of 303 S cm^{-1} at 700°C, arising from the mixed valence states of Pr^{3+}/Pr^{4+}, Ni^{2+}/Ni^{3+}, and Co^{2+}/Co^{3+}, as confirmed by X-ray photoelectron spectroscopy (XPS). The average thermal expansion coefficient (TEC) of PNCO was 16.5 × 10^{-6} K^{-1}. A fabricated NiO–8YSZ|8YSZ|PNCO button cell exhibited a peak power density of 78 mW cm^{-2} at 800 °C in fuel cell mode and produced 0.732 sccm cm^{-2} of H_2 in electrolyzer mode. Notably, the PNCO oxygen electrode exhibited a polarization resistance of 14.06 Ω cm^2, nearly three times lower than that of the conventional lanthanum strontium manganite (LSM) oxygen electrode (53 Ω cm^2) measured under identical conditions. These results demonstrate that PNCO is a highly active mixed ionic–electronic conductor (MIEC). Furthermore, reactivity studies between PNCO and 8YSZ conducted at 1150 °C for 2 h, reported here for the first time, revealed the formation of NiO and tetragonal ZrO_2 phases.

Keywords. Oxygen electrode; RSOFC; PNCO; power density; electrolyzer.

1. Introduction

Climate change, driven by the enhanced greenhouse effect resulting primarily from the increased combustion of fossil fuels, has emerged as one of the most significant environmental challenges facing humanity [1]. Consequently, the contribution of renewable energy sources has increased substantially to reduce dependence on fossil fuels and mitigate CO_2 emissions. This transition has created an urgent need for efficient energy conversion and storage technologies [2,3]. Accordingly, both emerging companies and established energy-sector industries are investing heavily in fuel cell technologies to address the intermittency of renewable energy sources and accelerate their commercial deployment [4].

Among the various fuel cell technologies, solid oxide fuel cells (SOFCs) have attracted considerable research and technological interest because of their high efficiency, fuel flexibility, and environmental compatibility. SOFCs employ ceramic materials and typically operate at temperatures between 600 and 1000 °C. They also offer flexibility in cell and stack design and can utilize a variety of fuels, including H_2, CO, and hydrocarbons [5]. Hydrogen is widely regarded as a clean and sustainable energy carrier, with water electrolysis representing one of the most promising technologies for its production. In addition, SOFCs can operate in reverse mode as solid oxide electrolysis cells (SOECs), providing an efficient route for hydrogen production. Consequently, increasing attention has been devoted to reversible solid

Supplementary Information: The online version contains supplementary material available at https://doi.org/10.1007/s12034-026-03752-y.

oxide fuel cells (RSOFCs), which can operate in both fuel cell and electrolysis modes, thereby enabling electricity generation and hydrogen production within the same device. Among the available hydrogen-production technologies, high-temperature steam electrolysis using RSOFCs is considered one of the most efficient and promising approaches. In SOEC mode, steam is supplied to the hydrogen electrode, where it is electrochemically reduced to produce hydrogen, while oxygen ions are transported through the electrolyte to the oxygen electrode, where oxygen is evolved [6]. The materials employed in SOECs are generally similar to those used in SOFCs.

In recent years, considerable effort has been directed toward developing self-sustaining RSOFC systems capable of achieving high electrolysis rates while producing hydrogen that can subsequently be used for electricity generation without an external hydrogen supply [2]. In conventional mixed ionic–electronic conductors (MIECs), the oxygen reduction reaction (ORR) and oxygen evolution reaction (OER) are largely confined to the triple-phase boundary (TPB), thereby limiting the electrochemically active region. Furthermore, alkaline-earth-containing oxygen electrode materials, particularly those containing Sr and Ba, exhibit a strong affinity for CO_2, which can lead to carbonate formation and consequent degradation in electrochemical performance. Examples include $La_{0.6}Sr_{0.4}Co_{0.2}Fe_{0.8}O_{3-\delta}$ and $Ba_{0.5}Sr_{0.5}Co_{0.8}Fe_{0.2}O_{2-\delta}$ [7]. Representative oxygen electrode materials investigated for SOFCs and SOECs include $La_{0.6}Sr_{0.4}Co_{0.2}Fe_{0.8}O_{3-\delta}$ [8], $La_{0.8}Sr_{0.2}MnO_{3-\delta}$ [8], $PrBa_{0.5}Sr_{0.5}Co_{1.5}Fe_{0.5}O_{5+\delta}$ [9], $La_{0.5}Sr_{0.5}FeO_{3-\delta}$ [10], $Nd_2NiO_{4+\delta}$ [11], and $Nd_{1.95}NiO_{4+\delta}$ [12].

Among the various oxygen electrode materials, $PrNi_{0.5}Co_{0.5}O_{3-\delta}$ (PNCO) has attracted considerable attention because its electrical conductivity is largely unaffected by moisture and its chemical stability is maintained in the presence of H_2O and CO_2 [2,7]. Spin-polarized density functional theory (DFT) calculations have shown that substituting 50% of the Co sites with Ni lowers the oxygen vacancy formation energy [3]. Furthermore, PNCO is a ferromagnetic semiconductor with a band gap of 1.05 eV [2]. A button cell incorporating a PNCO oxygen electrode and a $BaCe_{0.4}Zr_{0.4}Y_{0.1}Yb_{0.1}O_3$ electrolyte exhibited a peak power density of 528 mW cm^{-2}, while achieving an electrolysis current density of 1.31 A cm^{-2} at an applied voltage of 1.4 V and 600 °C [2]. Substituting Ni for 50% of the Co sites in $PrCoO_{2-\delta}$ also enhances proton transport by reducing the proton migration energy. PNCO synthesized by the Pechini method exhibited a high electrical conductivity of approximately 300 S cm^{-1} between 400 and 600 °C [7]. In comparison, other Pr-based electrodes, such as Pr_6O_{11} ($\sim$1.3 S cm^{-1} at 600 °C) [13], and Ba-based electrodes, such as $Ba_{0.95}La_{0.05}Fe_{0.9}Nb_{0.1}O_{3-\delta}$ ($\sim$4.91 S cm^{-1} at 650 °C) [14], exhibit significantly lower conductivities. However, symmetric cells employing PNCO electrodes with a proton-conducting $BaZr_{0.4}Ce_{0.4}Y_{0.1}Yb_{0.1}O_{2-\delta}$ (BZCYYb4411) electrolyte showed performance degradation due to H_2O and CO_2 poisoning [7]. In contrast, cells incorporating an oxygen-ion-conducting $Ce_{0.9}Gd_{0.1}O_{2-\delta}$ (GDC) electrolyte exhibited improved stability without such poisoning effects [7]. Further investigations using dilatometry and *in situ* XRD revealed minimal changes in the PNCO diffraction pattern, indicating that PNCO itself remains chemically stable in the presence of H_2O and CO_2 [7]. These observations suggest that the degradation observed in BZCYYb-based systems originates primarily from the electrolyte rather than the PNCO electrode.

Although previous studies have primarily focused on PNCO thin films or proton-conducting electrolytes in anode-supported, fuel-cell-only configurations [2], often incorporating additional interlayers [15], no studies have reported the use of PNCO as the oxygen electrode on an 8YSZ electrolyte in an electrolyte-supported, interlayer-free configuration for dual-mode RSOFC/SOEC operation. Electrolyte-supported 8YSZ cells provide excellent mechanical stability and gas tightness, thereby minimizing fuel/oxidant crossover, enabling accurate open-circuit voltage measurements, and improving fuel utilization during RSOFC/SOEC operation [16]. Eliminating the interlayer also simplifies cell fabrication. Previous studies have reported that the absence of an interlayer can reduce processing complexity, decrease interfacial resistance, and enhance oxygen reduction reaction kinetics by eliminating additional interfacial impedance [17,18]. Among the various chemical synthesis routes, the solution combustion method (SCM) is particularly attractive because it is simple, rapid, and cost-effective [19–21]. In the present study, PNCO powder was synthesized by SCM using citric acid as the fuel. The synthesized powder was employed as the oxygen electrode in a 1 cm^2 thick-electrolyte-supported button cell without an interlayer. The electrochemical performance of the cell was evaluated in both fuel cell and electrolyzer modes, and the chemical compatibility between PNCO and 8YSZ was also investigated.

2. Experimental

2.1 *Synthesis of the PNCO oxygen electrode powder by the solution combustion method*

r$Ni_{0.5}Co_{0.5}O_{3-\delta}$ (PNCO) powder was synthesized by the solution combustion method (SCM). Praseodymium oxide (Pr_6O_{11}, 99.9%, Mincometsal; 68.72 g) was first dissolved in nitric acid (HNO_2, 70%, Sigma-Aldrich). Subsequently, nickel nitrate hexahydrate ($Ni(NO_2)_2{\cdot}6H_2O$, 99%, Loba Chemie; 58.68 g), cobalt nitrate hexahydrate ($Co(NO_2)_2{\cdot}6H_2O$, 98%, Loba Chemie; 58.72 g), and citric acid monohydrate ($C_6H_8O_7{\cdot}H_2O$, 99.5%, Iso Chem; 117.81 g) were added in the stoichiometric proportions required for PNCO synthesis [21]. Citric acid was selected as the fuel because of its relatively low heat of combustion, which

promotes a smoldering combustion process and results in the formation of soft agglomerates. The resulting solution was continuously stirred and heated on a hot plate until a clear, homogeneous solution was obtained. The solution was then transferred to alumina crucibles and placed in a muffle furnace preheated to 400 °C for 2 h. During heating, the viscous gel underwent spontaneous combustion, releasing large volumes of gases and producing a porous, foamy PNCO powder with soft agglomerates and a high surface area. Finally, the powder was calcined at 800 °C for 4 h to remove residual carbonaceous species [19].

2.2 *Characterization*

The phase purity of the SCM-synthesized PNCO powder was examined by powder X-ray diffraction (XRD; Bruker D8 Advance) using Cu Kα radiation (λ = 1.5405 Å) with a Ni filter. Diffraction patterns were collected over a 2θ range of 20–60° at a scan rate of 2° min^{-1}. The crystallite size was estimated using the Scherrer equation [22].

Rietveld refinement of the synthesized PNCO powder and the reactivity-tested samples was performed using the PROFEX software package to determine the phase composition and identify any secondary phases. The morphology and elemental distribution of the synthesized powder were characterized by field-emission scanning electron microscopy (FESEM; Supra 40 VP, Carl Zeiss) equipped with an energy-dispersive X-ray spectroscopy (EDS; Oxford Instruments) detector. The particle-size distributions of the calcined and sintered powders were measured using a Mastersizer 2000 particle-size analyzer (Malvern).

The adiabatic flame temperature during solution combustion synthesis was estimated from the stoichiometric redox balance between the metal nitrates (oxidizers) and citric acid (fuel). Assuming complete combustion to gaseous products (CO_2, H_2O, N_2, and atmospheric O_2), the flame temperature was calculated from the reaction enthalpy and the heat capacities of the gaseous products. This calculation was performed to verify that the selected fuel-to-oxidizer ratio provided sufficient thermal energy for the formation of crystalline PNCO. Furthermore, citric acid was selected to maintain a relatively low combustion temperature, thereby minimizing excessive grain growth and producing fine, highly reactive, weakly agglomerated powders with good sinterability for oxygen electrode applications [20,21].

The oxidation states of the constituent elements were investigated by X-ray photoelectron spectroscopy (XPS; SPECS) using PNCO pellets prepared from powder calcined at 800 °C for 4 h. The spectra were analyzed using CASA XPS software. Oxygen non-stoichiometry (δ) was determined because oxygen vacancies strongly influence the structural stability, electrical conductivity, and catalytic activity of solution combustion-synthesized PNCO.

For iodometric titration, 0.1 g of finely ground PNCO powder (calcined at 800 °C for 4 h) was accurately weighed into a 250 mL conical flask and dissolved in 20 mL of hydrochloric acid (35–38%, 1.18 specific gravity, BP/Ph. Eur., SD Fine Chem Ltd.) under gentle heating until a clear solution was obtained. After cooling to room temperature, approximately 0.5 g of potassium iodide (KI, 99.5%, Iso Chem) was added, and the solution was stirred until a uniform brown color developed. The liberated iodine was titrated with standardized 0.1 M sodium thiosulfate pentahydrate ($Na_2S_2O_3{\cdot}5H_2O$, 99%, SD Fine Chem Ltd.) until the solution became pale yellow. Subsequently, 5 mL of freshly prepared starch indicator solution (soluble potato starch, Loba Chemie) was added, producing an intense blue color, and the titration was continued until the blue color disappeared, which was taken as the endpoint. At least three titrations were performed for each sample, and the average value was used. The oxygen non-stoichiometry (δ) was calculated from the sodium thiosulfate consumption according to the standard redox stoichiometry between I_2 and $S_2O_3^{2-}$ [23,24].

For electrical conductivity measurements, 8 g of PNCO powder was granulated with four drops of 6 wt.% polyvinyl alcohol (PVA) binder and pressed into pellets using a hydraulic press (VK Instruments, Bangalore) under a load of 75 kN. The green pellets were sintered at 1150 °C for 2 h. The bulk density and apparent porosity of the sintered pellets were determined using Archimedes' principle. Electrical conductivity was measured using the Van der Pauw four-probe DC method with a Keithley 6221 current source (100 mA) and a Keithley nanovoltmeter. Four silver-wire contacts were attached to the pellet using silver paste. The samples were dried and heated at 800 °C for 30 min to improve adhesion of the silver contacts before conductivity measurements were performed.

The thermal expansion coefficient (TEC) of the PNCO pellets (12 mm diameter and 4 mm thickness) was measured from room temperature to 800 °C in air using a home-built dilatometer at a heating rate of 5 °C min^{-1}. For pellet preparation, 20 g of PNCO powder was mixed with ten drops of polyvinyl alcohol (PVA), pressed at 140 kN for 60 s using a hydraulic press (VB Ceramics, Chennai), and sintered in air at 1150 °C for 2 h.

To evaluate the chemical compatibility between the PNCO oxygen electrode and the 8YSZ electrolyte, equal amounts (1 g each) of PNCO and 8YSZ powders were thoroughly mixed and ground for 20 min. Approximately 60 drops of deionized water were then added, and grinding was continued for an additional 30 min. The resulting paste was dried under an infrared lamp, reground for 15 min, and heat-treated in air at 1150 °C for 2 h in a home-built furnace. The

reacted powders were subsequently analyzed by XRD to evaluate phase stability and identify any reaction products.

2.3 *Button cell fabrication and testing*

Electrolyte tapes of 8 mol% yttria-stabilized zirconia (8YSZ, Tosoh Corporation) were prepared by mixing 80 g of 8YSZ powder with optimized amounts of Menhaden fish oil as the dispersant and ethanol and toluene as co-solvents. The slurry was initially ball-milled with zirconia balls for 24 h using a roller mill. Subsequently, benzyl butyl phthalate and polyvinyl butyral were added as the plasticizer and binder, respectively, and the slurry was further ball-milled for an additional 24 h to ensure homogeneity. Finally, a few drops of polyalkylene glycol were added as a rheological modifier, and the slurry was milled for approximately 5 h.

The homogeneous slurry was tape-cast onto Mylar sheets using an in-house-built tape caster to obtain green 8YSZ tapes with a thickness of approximately 220 μm, followed by drying at room temperature for several hours. Twenty tape layers (30 mm diameter) were stacked and uniaxially pressed at 90 kN using a hydraulic press. The laminated electrolyte was then sintered in air at 1500 °C for 2 h, followed by cooling at 3 °C min^{-1}, to achieve a density close to the theoretical value. The resulting electrolyte pellet had a thickness of approximately 818 μm, as confirmed by FESEM.

The fuel electrode paste was prepared by mechanically mixing NiO powder (99.9%, Inframat) and 8YSZ powder (Tosoh Zirconia TZ-8Y) in a weight ratio of 62.5:37.5, together with ethyl cellulose (Loba Chemie) and terpineol (80%, Loba Chemie). The mixture was ground using a mortar and pestle to obtain a paste of suitable viscosity for screen printing. The NiO–8YSZ paste was screen-printed (Sudharshan Printline) onto one side of the sintered 8YSZ electrolyte over an active area of 1 cm^2 and subsequently sintered at 1300 °C for 2 h to produce the half-cell.

The oxygen electrode paste was prepared in a similar manner using 15 g of calcined PNCO powder, ethyl cellulose, and terpineol. The paste was screen-printed onto the opposite side of the half-cell over an active area of 1 cm^2 and sintered in air at 1150 °C for 2 h to obtain an asymmetric full cell with the configuration NiO–8YSZ (~33 μm) | 8YSZ (~820 μm) | PNCO (~37 μm).

The electrochemical performance of the fabricated button cells was evaluated using a fuel cell test station (Fuel Cell Technologies, Inc., USA). A relatively thick electrolyte was employed because of limitations associated with the button-cell test setup. The button cell was sealed to an alumina tube using Aremco ceramic sealant and mounted in a Probostat button-cell test fixture (supplementary figure S1) for electrochemical characterization. The ceramic sealant was cured in air at 800 °C with a heating rate of 3 °C min^{-1}. During fuel cell testing, pure hydrogen (150 sccm) and oxygen (100 sccm) were supplied continuously to the fuel and oxygen electrodes, respectively.

Electrochemical impedance spectroscopy (EIS) measurements were performed using a CHI604D electrochemical workstation under open-circuit voltage (OCV) conditions with an AC perturbation amplitude of 10 mV over a frequency range of 1 MHz to 0.1 Hz. The cell was subsequently operated in electrolyzer mode by applying a constant current density of 0.5 A cm^{-2} at 800 °C, using a gas composition of 50% H_2O/50% H_2 at the fuel electrode and air at the oxygen electrode. Under these conditions, the OCV remained stable at approximately 1.08 V. The amount of hydrogen generated was calculated using the following equation:

$$V = \frac{I \times t}{n \times F} \times 22.4\,L\,mol^{-1} \quad (1)$$

where I is the current (A), T is the electrolysis time (s), N is the number of electrons required to produce one mole of hydrogen, and F is Faraday's constant (96,485 C mol^{-1}). After electrochemical testing, the button cell was sectioned, mounted in epoxy resin, and polished for cross-sectional microstructural analysis.

3. Results and discussion

3.1 *X-ray diffraction analysis*

Figure 1a–d illustrates the XRD patterns and Rietveld refinement analysis of the PNCO powder, sintered pellets, and chemical compatibility samples. The XRD patterns of the PNCO powder and sintered pellets are shown in figure 1a, revealing sharp diffraction peaks characteristic of well-crystallized materials. After sintering at 1150 °C, the crystallite size increased from approximately 29 to 39 nm, indicating significant grain growth. The lattice parameters obtained from the Rietveld refinement (a = 5.40 Å, b = 5.39 Å, and c = 7.63 Å) confirm that the material crystallized as a single-phase orthorhombic perovskite, in excellent agreement with the standard JCPDS card (No. 25-1069), with no detectable secondary phases. As summarized in table 1, the Rietveld refinement yielded a weighted profile R-factor (R_{wp}) of 2.05% and a goodness-of-fit (GoF) value of 1.33, indicating excellent agreement between the calculated and experimental diffraction patterns. This high degree of agreement is evident in figure 1b, where the observed pattern (red line) and the calculated pattern (blue line) exhibit excellent overlap. The low intensity of the difference curve (yellow line) and the close alignment of the Bragg reflection positions (green vertical bars) further confirm the phase

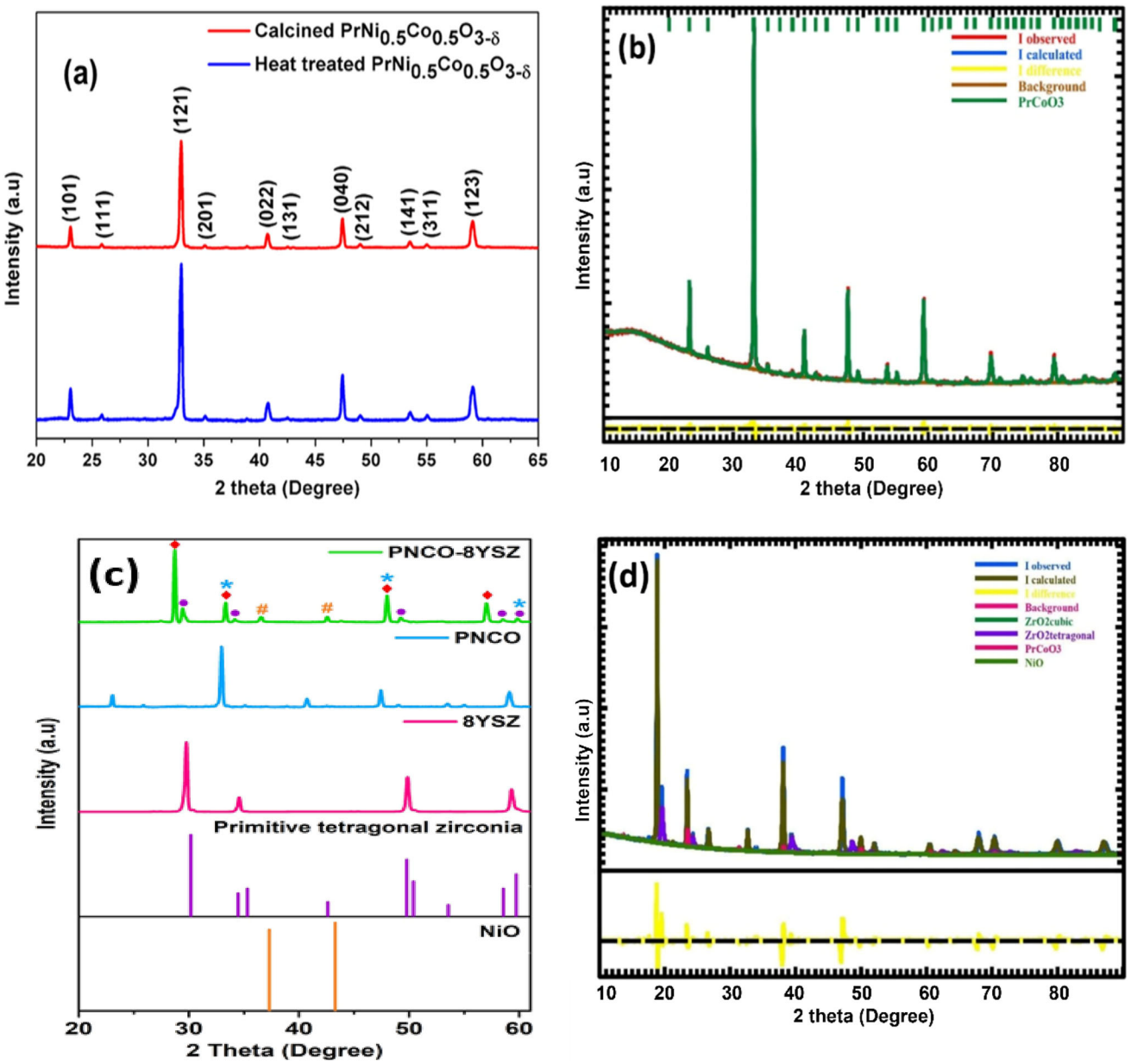

Figure 1. (**a**) X-ray diffraction (XRD) pattern of the PNCO powder calcined at 800 °C for 4 h and the PNCO pellet sintered at 1150 °C for 4 h; (**b**) Rietveld refinement of the PNCO powder calcined at 800 °C for 4 h; (**c**) XRD pattern of the PNCO + 8YSZ sample after the reactivity study; and (**d**) Rietveld refinement of the reactivity mixture sintered at 1150 °C for 2 h.

purity and structural integrity of the synthesized PNCO powder.

The XRD pattern of the 50 wt.% PNCO–50 wt.% 8YSZ mixture after the chemical compatibility test at 1150 °C is shown in figure 1c. Although the major diffraction peaks of both constituents are retained, the analysis indicates partial phase transformation of cubic YSZ to a primitive tetragonal phase, as evidenced by the appearance of new reflections at 29.5° and 34.07°. In addition, diffraction peaks at 36.51° and 42.55° are assigned to NiO, confirming that a chemical reaction occurred during heat treatment. This increased structural complexity is reflected in table 2, where the PNCO–8YSZ mixture exhibits a higher Rwp value (5.80%) and a GoF of 4.2 compared with those of the pure PNCO sample. The corresponding multiphase Rietveld refinement is presented in figure 1d. The refinement demonstrates successful indexing of the secondary phases, with the calculated model accounting for the primitive tetragonal zirconia, NiO, and the remaining PNCO phase. Although the residual values are higher because of peak overlap among

Table 1. Rietveld refinement parameters of the PNCO powder calcined at 800 °C for 4 h.

Parameters	Value
a	5.40 Å
b	5.39 Å
c	7.63 Å
R_{wp}	2.05 %
R_{exp}	1.53 %
χ^2	1.79 %
GoF	1.33

Table 2. Rietveld refinement parameters of the reactivity-tested sample and the parent PNCO electrode.

Samples	R_p	R_{wp}	GoF	χ^2
PNCO	1.17	3.46	2.9	8.74
8YSZ-PNCO	1.37	5.80	4.2	9.40

the reaction products, the relatively small difference curve (yellow line) indicates that the multiphase model provides a satisfactory fit to the experimental diffraction data.

Although these reaction products form during bulk heat treatment, they are unlikely to form extensively at the electrode–electrolyte interface under the present fabrication conditions and are therefore not expected to significantly degrade the overall electrochemical performance of the cell. Furthermore, no secondary insulating zirconate phases (e.g., Ni- or Co-zirconates) were detected, suggesting the absence of detrimental interfacial reactions. The formation of the tetragonal zirconia phase is likely associated with local redistribution of yttria within YSZ, a well-known phenomenon that is not generally considered detrimental. Similar interdiffusion has been reported in conventional LSM–YSZ systems, where performance degradation is primarily attributed to the formation of insulating zirconate phases rather than interdiffusion itself [25]. Even after prolonged operation, LSM–YSZ cells generally maintain stable electrochemical performance despite limited interdiffusion, indicating that such interfacial changes are tolerable. Therefore, the phase evolution observed in the present study is unlikely to adversely affect the electrochemical performance or long-term stability of the PNCO/8YSZ electrode–electrolyte system.

3.2 *FESEM analysis*

The FESEM images of the calcined and sintered PNCO powders are shown in figure 2a,b. The calcined powder consists of particles with both spherical and elongated rod-like morphologies, which are likely formed through agglomeration during the calcination process. After sintering at 1150 °C, the particles become larger and more irregular because of grain growth and densification, as shown in figure 2b. The EDS analysis of the calcined and sintered PNCO powders is summarized in table 3. The elemental composition of the PNCO powder calcined at 800 °C for 4 h agrees well with the theoretical composition.

The elemental maps of the calcined PNCO powder (figure 2c) show a uniform distribution of the constituent elements, whereas the sintered powder (figure 2d) exhibits slight agglomeration. The calcined powder displays a highly porous, interconnected network composed of fine nanostructured grains. Higher-magnification images reveal primary particles with sizes ranging from 0.1 to 0.2 μm, which are favorable for high-surface-area applications such as catalysis [24,26]. After sintering at 1150 °C for 2 h, a significant microstructural evolution is observed. The increased thermal energy promotes grain growth and densification, resulting in the formation of larger, discrete agglomerates. The increase in the image scale from 0.2 to 2 μm further illustrates the transition from a nanostructured powder to a more chemically stable microstructured ceramic [24].

The EDS analysis indicates that the measured Co content is lower in the sintered powder than in the calcined powder (table 3). This reduction may be attributed to partial volatilization of Co at the elevated sintering temperature as a result of its increased vapor pressure [27]. Consequently, the measured Ni content appears relatively higher because of the corresponding decrease in the Co content (table 3).

3.3 *Particle size analysis*

Supplementary figure S2a–d presents the particle-size distribution curves and corresponding histograms of the calcined and sintered PNCO powders. The particle-size distribution of the powder calcined at 800 °C for 4 h exhibits a bimodal distribution with $d_{0.1}$ = 0.09 μm, $d_{0.5}$ = 0.24 μm, and $d_{0.9}$ = 2.30 μm (supplementary figure S2a). In contrast, the powder sintered at 1150 °C for 2 h also exhibits a bimodal distribution but with significantly larger particle sizes, having $d_{0.1}$ = 2.11 μm, $d_{0.5}$ = 5.27 μm, and $d_{0.9}$ = 18.83 μm (supplementary figure S2b). Consequently, the median particle size ($d_{0.5}$) increased from 0.24 to 5.27 μm after sintering, reflecting substantial grain growth during heat treatment.

A bimodal particle-size distribution is advantageous for SOFC applications because the finer particles provide a high specific surface area and increase the number of active sites available for the oxygen reduction reaction (ORR). In contrast, the coarser particles facilitate gas transport by creating more open and interconnected pore channels, thereby reducing concentration polarization and improving gas diffusivity [20]. For example, the power density of an

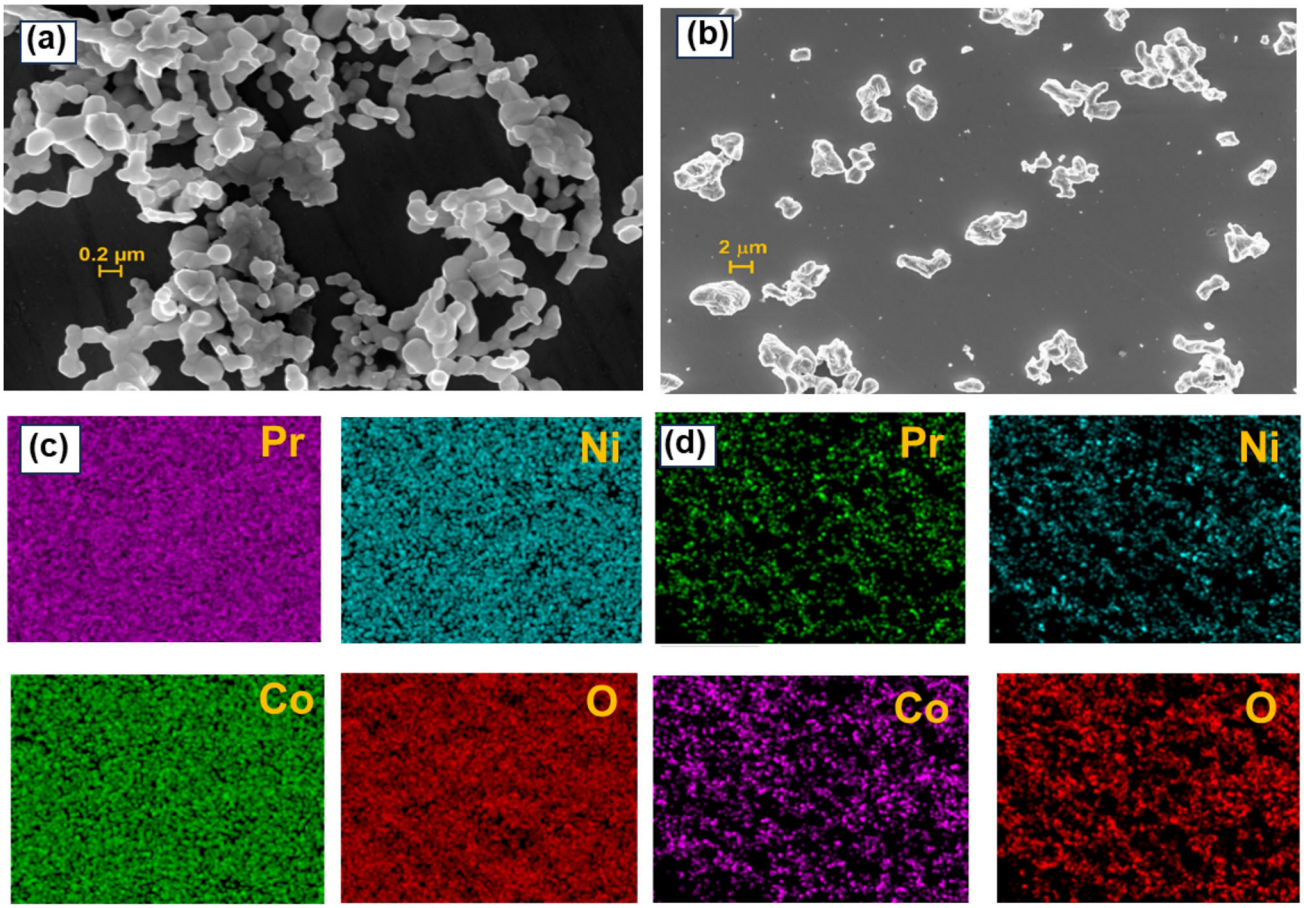

Figure 2. Field-emission scanning electron microscopy (FESEM) images of the PNCO powder: (**a**) 50 kX magnification after calcination at 800 °C for 4 h and (**b**) 5 kX magnification after sintering at 1150 °C for 2 h; and X-ray elemental maps of the PNCO powder (**c**) after calcination at 800 °C for 4 h and (**d**) after sintering at 1150 °C for 2 h.

Table 3. EDS analysis of calcined and sintered PNCO powders.

Element	Calculated wt%	Calcined		Sintered	
		Observed wt.%	Deviation %	Observed wt.%	Deviation %
Pr	64.3	65.1	0.7	64.2	2.3
Ni	17.8	17.1	0.7	19.1	3.6
Co	17.8	17.9	0.1	16.6	1.1

SOFC employing an LSM oxygen electrode increased from 132 to 228 mW cm^{-2} when a bimodal particle-size distribution was used [28]. Therefore, combining fine and coarse particles in a bimodal distribution can improve the overall electrocatalytic performance of the oxygen electrode [29,30].

The particle-size histograms were generated from FESEM images using ImageJ software. As shown in supplementary figure S2c, most particles in the calcined powder fall within the size range of 0.25–0.30 µm. After sintering, the particle-size distribution shifts to larger sizes, with most particles falling within the range of 5.0–5.5 µm (supplementary figure S2d). This observation is in good agreement with the median particle size obtained from the particle-size analysis.

3.4 *Adiabatic flame temperature calculations*

In solution combustion synthesis, the combustion temperature strongly influences the crystallite size, which generally increases with increasing combustion temperature [4,21].

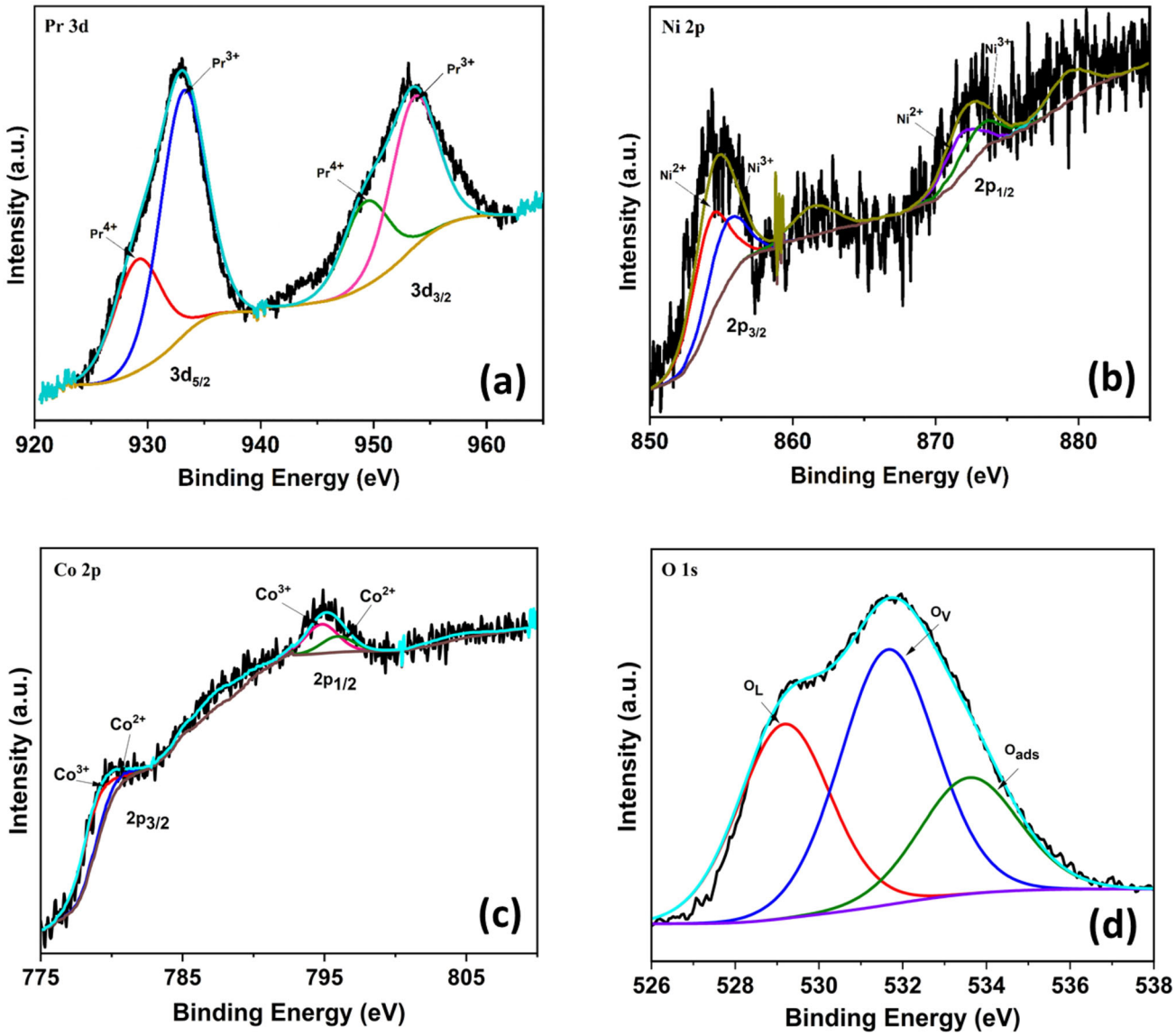

Figure 3. X-ray photoelectron spectroscopy (XPS) core-level spectra of the PNCO powder calcined at 800 °C: (**a**) Pr 3D, (**b**) Ni 2P, (**c**) Co 2P, and (**d**) O 1S.

The maximum temperature attained during the combustion reaction is referred to as the adiabatic flame temperature (T_{ad}). The heat released during the combustion process corresponds to the enthalpy of the reaction. Assuming complete combustion, the overall reaction between praseodymium oxide, nitric acid, nickel nitrate, cobalt nitrate, and citric acid to produce PNCO powder can be expressed as follows:

$$\begin{aligned} &Pr(NO_3)_3\ .6H_2O + \ 0.5\ Ni(NO_3)_2\ .6H_2O \\ &+ 0.5\ Co(NO_3)_2 6H_2O \\ &+ \ 1.39\ C_6H_8O_7H_2O \xrightarrow{Air} \ PrNi_{0.5}Co_{0.5}O_{3-\delta} \\ &+ 8.33\ CO_2 + 18.95\ H_2O + 2.5\ N_2 \end{aligned} \quad (2)$$

The combustion reaction occurs over a very short duration, during which exceptionally high temperatures are attained. The adiabatic flame temperature can be estimated using the equations reported in the literature [4,20] together with the thermodynamic data listed in supplementary table S1. The values of $\Delta H_{f\ (Reactant)}$, $\Delta H_{f\ (Product)}$, ΔH°, and ΔnC_p were calculated to be −7275.0, −9059.9, −1784.9 kJ mol^{-1}, and 1138.9 J K^{-1}, respectively. Based on these values, the calculated adiabatic flame temperature for the citric acid–nitrate combustion system was 1567 °C (1865 K). Although the self-propagating combustion reaction lasts only a few seconds, the citric acid–nitrate system produces phase-pure PNCO powder [20]. While the redox mixture is ignited in a preheated muffle furnace at approximately 400 °C, the combustion temperature is substantially higher because of the exothermic redox reaction. During combustion, a significant fraction of the released heat is dissipated to the surroundings through the evolution of gaseous reaction products [20].

3.5 *X-ray photoelectron spectroscopy (XPS) analysis*

The XPS spectra of the PNCO perovskite powder synthesized by the solution combustion method and calcined at 800 °C are shown in figure 3a–d. The spectra were deconvoluted using Gaussian functions in CASA XPS software to identify the oxidation states of Pr, Ni, Co, and O.

As shown in figure 3a, the Pr 3d spectrum consists of two broad spin–orbit components corresponding to the Pr $3d_{5/2}$ and Pr $3d_{3/2}$ states, indicating the coexistence of Pr^{3+} and Pr^{4+} at the surface. The Pr $3d_{5/2}$ region (925–937 eV) contains a dominant peak at 930–935 eV assigned to Pr^{4+}. This intense feature is characteristic of oxidized Pr in perovskites and results from efficient screening of the 3d core hole by oxygen 2p valence electrons [7,31–33]. The satellite peak at 925–930 eV is attributed to the Pr^{3+} state and arises from a poorly screened final state following photoemission [32–34]. The Pr $3d_{3/2}$ component occurs at 950–955 eV, with a spin–orbit splitting of approximately 20–21 eV relative to the $3d_{5/2}$ peak, consistent with previously reported values for Pr-containing oxides [35]. The satellite feature at 945–950 eV is similarly associated with an unscreened final state, while the weak feature at 955–960 eV is attributed to plasmon-loss excitations or coupling between the core hole and the unpaired 4f electron of Pr^{4+} [31–36].

The coexistence of Pr^{3+} and Pr^{4+} is beneficial for electrochemical performance. Pr^{3+} promotes oxygen-vacancy formation and enhances mixed ionic–electronic conduction (MIEC), thereby facilitating the oxygen reduction and oxygen evolution reactions (ORR/OER). In contrast, Pr^{4+} contributes to electronic conductivity through the Pr^{4+}/Pr^{3+} redox couple and improves the structural stability of the perovskite during redox cycling [37].

The Ni 2p spectrum (figure 3b) reveals the coexistence of Ni^{2+} and Ni^{3+} species, with binding energies of 872.08 and 873.07 eV, respectively, together with characteristic satellite features at 879.4 eV [38]. The presence of Ni^{2+} facilitates oxygen-vacancy formation through charge compensation, thereby extending the electrochemically active region and enhancing the ORR [39]. Meanwhile, the Ni^{3+}/Ni^{2+} redox couple increases hole concentration, improves p-type electronic conductivity, and further promotes oxygen-vacancy formation [40].

The Co 2p spectrum (figure 3c) also exhibits mixed oxidation states. The peak at 779.99 eV is assigned to octahedrally coordinated low-spin Co^{3+} occupying the perovskite B-site [33,38]. A second component at 784.84 eV is attributed to surface Co^{2+} formed through partial reduction of Co^{3+} during calcination via oxygen-vacancy formation [41]. The weak satellite at 787.5 eV corresponds to a charge-transfer shake-up feature characteristic of low-spin Co^{3+} [38,41]. In the Co $2p_{1/2}$ region, peaks corresponding to Co^{2+} and Co^{3+} are observed at 780.80 and 796.06 eV, respectively. The coexistence of Co^{2+} and Co^{3+} facilitates small-polaron hopping between adjacent Co ions, resulting in high p-type conductivity. In addition, Co^{2+} promotes oxygen-vacancy formation, while Co^{3+} enhances oxygen electrocatalysis by facilitating lattice-oxygen participation in the ORR/OER, thereby improving MIEC [7,42].

The deconvoluted O 1s spectrum (figure 3d) consists of three components. The peak at 529.20 eV is assigned to lattice oxygen, confirming the integrity of the perovskite framework through strong metal–oxygen bonding [43]. The peak at 531.67 eV corresponds to oxygen vacancies and chemisorbed oxygen species, indicating the presence of catalytically active surface sites that facilitate vacancy-mediated oxygen-ion transport and improve the ORR/OER [44,45]. The higher-binding-energy peak at 533.63 eV is attributed to surface carbonates and adsorbed hydroxyl or water species. Its relatively low intensity suggests limited surface carbonation and is consistent with the reported CO_2

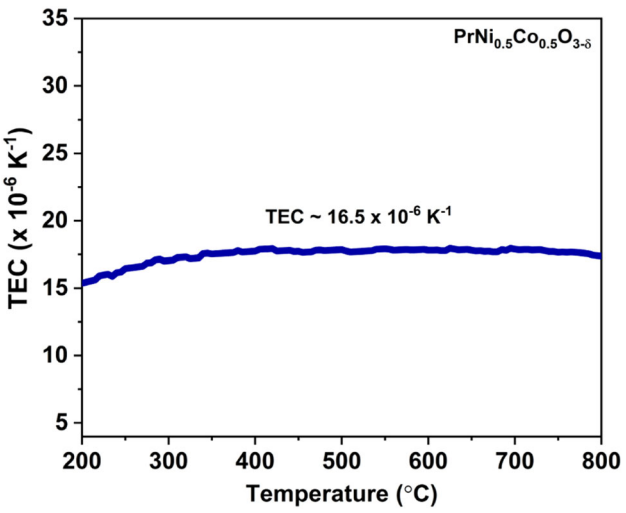

Figure 4. Thermal expansion coefficient as a function of temperature for the sintered PNCO sample.

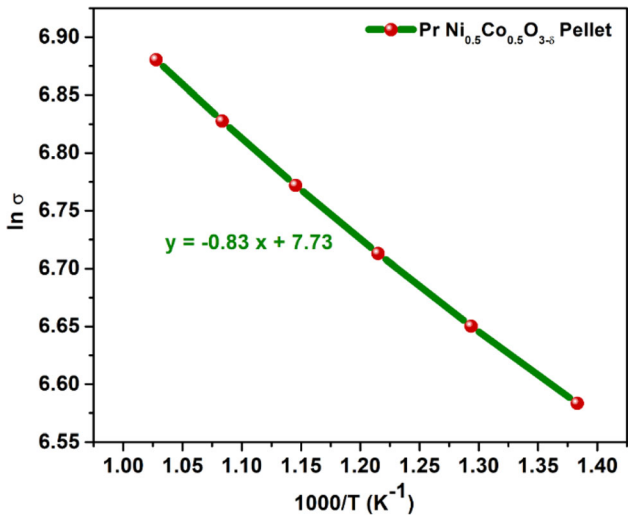

Figure 5. Electrical conductivity of the PNCO pellet sintered at 1150 °C for 2 h as a function of temperature.

tolerance of PNCO [46,47]. The relative peak intensities indicate a substantial concentration of surface oxygen species and hydroxyl groups, reflecting an electrochemically active surface. These observations are consistent with previous XPS studies of perovskite oxygen electrodes [36,48].

Furthermore, quantitative XPS analysis indicates mixed valency at the B-site, with Ni^{2+}/Ni^{3+} and Co^{3+}/Co^{2+} ratios of approximately 60/40 and 74/26, respectively. Together with the measured oxygen non-stoichiometry ($\delta \approx 0.09$), these mixed-valence cations (Pr^{3+}/Pr^{4+}, Ni^{2+}/Ni^{3+}, and Co^{2+}/Co^{3+}) indicate a highly dynamic redox-defect structure that is expected to promote oxygen-ion transport, electronic conductivity, and oxygen-electrode activity.

3.6 *Iodometric titration*

The calculated oxygen non-stoichiometry (δ) from iodometric titration is 0.09. This transition from $PrNi_{0.5}Co_{0.5}O_3$ to $PrNi_{0.5}Co_{0.5}O_{2.91}$ is not just a mass loss. This non-stoichiometry is crucial as it introduces oxygen vacancies that enable MIEC essential for efficient ORR at SOFC cathodes. The value of 0.09 aligns with the reported value of 0.085 at 600 °C [1]. In an ideal case, Ni and Co exist as Ni^{3+} and Co^{3+} on the B site. But at high temperatures, due to lattice vibrations during heat treatment, Ni^{3+} becomes unstable and prefers a lower oxidation state, breaking the metal-oxygen bond. Oxygen leaves the lattice; to maintain charge neutrality, two electrons (e^-) also leave. Because Ni^{3+} has a higher electron affinity, it will capture an electron to form Ni^{2+}. Once Ni has reduced, the Co^{3+} begins to reduce to Co^{2+} to compensate for the remaining oxygen vacancies. This creates a mixed-valence state of Ni and Co, as shown in the XPS spectra in figure 3b-c. This defect-driven chemistry promotes the triple conduction (O^{2-}, e^-, H^+) vital for high-performance perovskite cathodes.

The oxygen non-stoichiometry (δ) determined by iodometric titration was 0.09, corresponding to a composition of $PrNi_{0.5}Co_{0.5}O_{2.91}$. This oxygen deficiency is significant because it generates oxygen vacancies that promote mixed ionic–electronic conduction (MIEC), which is essential for efficient oxygen reduction reaction (ORR) kinetics in SOFC oxygen electrodes. The measured δ value is in good agreement with the reported value of 0.085 at 600 °C [1].

In the ideal perovskite structure, Ni and Co are expected to exist predominantly in the +3 oxidation state at the B-site. During heat treatment, however, elevated temperatures destabilize the higher oxidation states, resulting in oxygen loss from the lattice and the formation of oxygen vacancies. To maintain charge neutrality, a fraction of the Ni^{3+} ions is reduced to Ni^{2+}, followed by partial reduction of Co^{3+} to Co^{2+}. This process gives rise to the mixed-valence states of Ni and Co observed in the XPS spectra (figure 3b,c). The coexistence of oxygen vacancies with mixed-valence Ni^{2+}/Ni^{3+} and Co^{2+}/Co^{3+} redox couples facilitates both ionic and electronic charge transport, thereby enhancing the electrochemical activity of the PNCO oxygen electrode.

3.7 *Thermal expansion coefficient (TEC)*

The thermal expansion coefficient (TEC) curve of the sintered PNCO pellet, measured by dilatometry in air over the temperature range of 100–800 °C, is shown in figure 4. The TEC exhibits an approximately linear variation between 350 and 800 °C, with an average value of $16.5 \times 10^{-6}\ K^{-1}$, which is in good agreement with the reported literature value [7]. A 40% increase in the TEC is observed between 100 and 350 °C. This behavior is likely associated with spin-state transitions of Co^{3+} in the perovskite lattice, where Co^{3+} undergoes a transition from a low-spin to a high-spin state between approximately 200 and 400 °C. The accompanying increase in the ionic radius causes lattice expansion without a structural phase transition, thereby contributing to the observed increase in the TEC [30,31]. Similar spin-state transitions affecting the thermal properties of cobalt-containing perovskites have been reported previously [49].

Above 350 °C, the TEC becomes nearly constant. At these temperatures, thermal expansion is dominated by lattice vibrations, and the progressive excitation of phonon modes results in an approximately linear expansion with temperature. Such nonlinear thermal expansion behavior, characterized by an initial increase followed by a nearly constant TEC, is commonly observed in complex oxide ceramics.

The TEC is a critical parameter in the design of solid oxide fuel cells because thermal expansion mismatch between the electrode and electrolyte can generate mechanical stresses during thermal cycling [30,32]. Although the TEC of PNCO becomes stable above 350 °C, its relatively high value ($16.5 \times 10^{-6}\ K^{-1}$) may increase the likelihood of thermal stress and interfacial cracking when paired with electrolytes having significantly lower TEC values.

3.8 *Conductivity measurement*

The bulk density of the sintered PNCO pellet, determined by Archimedes' principle, was 7.70 g cm^3, with an apparent porosity of 0.2129%. The measured density was in good agreement with the theoretical density [50]. The temperature dependence of the electrical conductivity of the PNCO pellet sintered at 1150 °C for 2 h is presented as an Arrhenius plot (ln σ versus 1000/*T*) in figure 5. The excellent linear relationship indicates thermally activated conduction and confirms the semiconducting behavior of PNCO over the investigated temperature range [7,51].

The electrical conductivity increased from 187 S cm^{-1} at 500 °C to 303 S cm^{-1} at 700 °C, in good agreement with

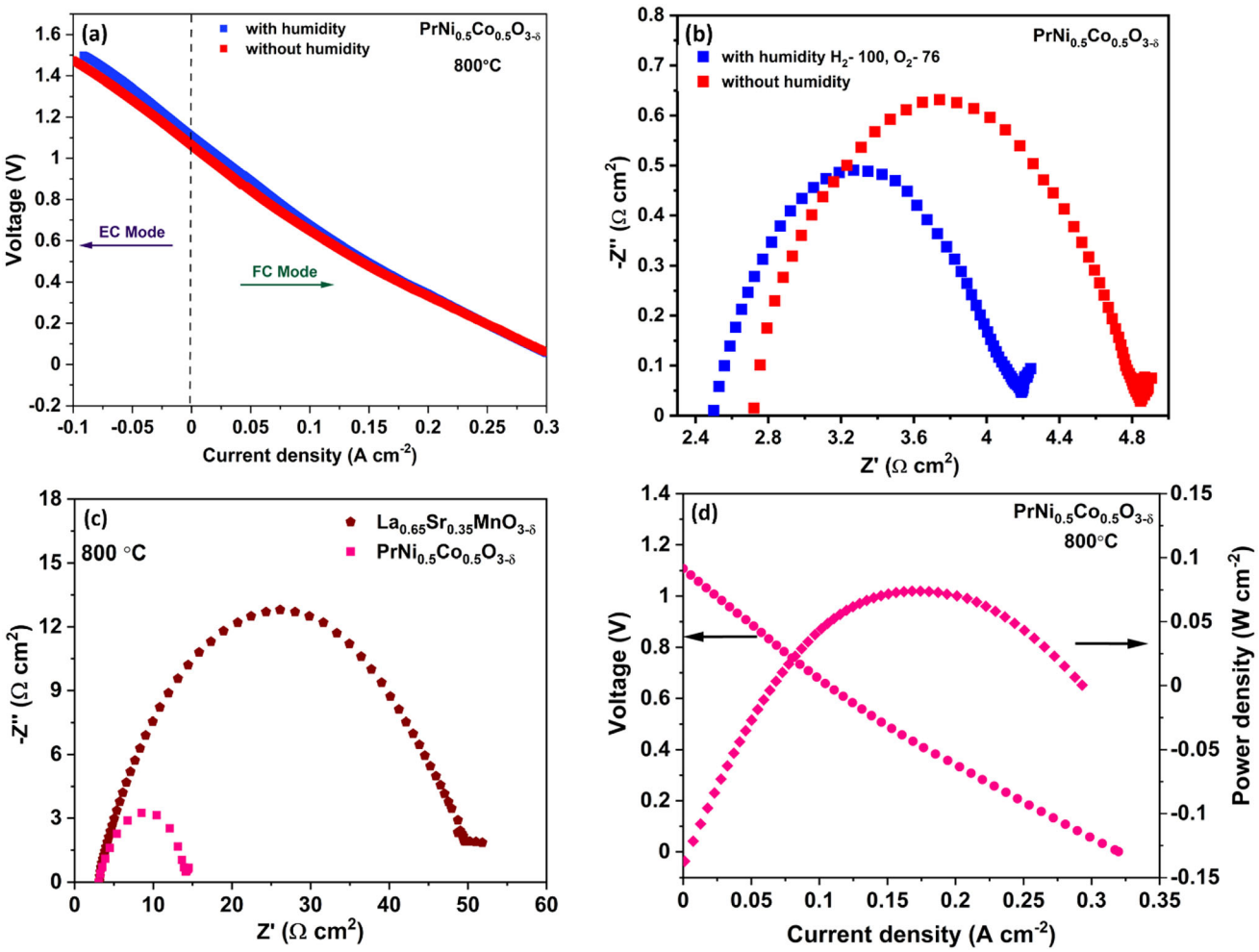

Figure 6. Electrochemical performance of the PNCO oxygen electrode with an 8YSZ electrolyte: (**a**) linear sweep voltammetry (LSV) curves measured with and without moisture, (**b**) electrochemical impedance spectroscopy (EIS) spectrum of the PNCO oxygen electrode, (**c**) comparison of the EIS spectra of the PNCO and conventional LSM oxygen electrodes, and (**d**) power density curve of the PNCO oxygen electrode with an 8YSZ electrolyte.

previously reported values [7]. These conductivity values are comparable to those of conventional oxygen electrode materials, such as $PrNiO_{4+\delta}$, $La_{0.8}Sr_{0.4}Co_{0.8}Fe_{0.2}O_{3-\delta}$ (LSCF), and $La_{0.8}Sr_{0.2}Fe_{0.2}Ni_{0.2}O_{3-\delta}$ (LSFN), and are substantially higher than those of several triple-conducting electrode materials, including $BaZr_{0.1}Ce_{0.7}Y_{0.1-x}Co_xO_{3-\delta}$ and $BaCo_{0.7}Fe_{0.2}Nb_{0.1}O_{3-\delta}$, which typically exhibit conductivities in the range of 0.1–10 S cm^{-1} at 600 °C [7].

The linear Arrhenius behavior is consistent with a thermally activated small-polaron hopping conduction mechanism, which is characteristic of Co-containing perovskite oxides [52]. The high electrical conductivity is advantageous because it minimizes ohmic losses, particularly under high-current operating conditions, thereby reducing resistive heating and improving cell efficiency. This property also facilitates efficient electron transport during both the oxygen reduction reaction (ORR) and oxygen evolution reaction (OER), making PNCO comparable to benchmark oxygen electrode materials such as LSCF. Furthermore, the relatively low activation energy (11.74 kJ mol^{-1}) indicates facile charge transport through the small-polaron hopping mechanism, which is expected to promote faster electrode kinetics and improved reversibility during both fuel cell and electrolysis operation [26,39,53].

3.9 *Enhanced ORR mechanism in PNCO*

Rare-earth nickelates, such as $PrNiO_{3-\delta}$, intrinsically exhibit small-polaron hopping, strong carrier localisation arising from Jahn–Teller distortion limits mobility and increases the activation barrier [54]. In contrast, partial substitution of Co incorporation enhances metal–oxygen covalency and introduces additional Co^{2+}/ Co^{3+} redox couples, thereby reducing the activation energy for hopping and increasing polaron density, thereby improving electronic conductivity [55].

Consequently, the Co^{2+}/ Co^{3+} redox couple is more energetically accessible and exhibits greater reversibility than the Ni^{2+}/Ni^{3+} pair. Pr^{3+} contributes to lattice flexibility and stabilizes oxygen vacancies, while Co enhances B-site redox activity and M-O covalency, lowering the activation barriers for both charge transfer and oxygen exchange. The predominance of Co^{3+} provides a highly oxidising surface that promotes oxygen adsorption and activation, while the coexistence of reduced species (Ni^{2+}, Co^{2+}) ensures continuous electron supply for ORR. Consequently, PNCO exhibits mixed ionic-electronic conduction, with contributions from O^{2-} and e^{-}. Further, under humid conditions, proton transport occurs in parallel via a Grotthuss-type hopping mechanism involving hydroxyl defects ($O\dot{H}_o$) on the oxygen sublattice [56].

Classical oxygen reduction reaction (ORR) in PNCO:

1. Oxygen adsorption
$$O_2(g) \rightarrow O_2(ads)$$
2. Electron transfer (via polaron hopping)
$$O_2(ads) + e^- \rightarrow O_2^-(ads)$$
$$O_2(ads) + e^- \rightarrow O_2^{2-}(ads)$$
3. Dissociation
$$O_2^{2-}(ads) \rightarrow 2O_o^{\cdot}(ads)$$
4. Final reduction to lattice oxygen
$$O_o^{\cdot} + e^- \rightarrow O_o^x$$
5. Vacancy incorporation (overall reaction)
$$\frac{1}{2}O_2(g) + V_o^{\cdot\cdot} + 2e^- \rightarrow O_o^x$$

Proton assisted ORR in in PNCO

Under moist conditions, parallel proton conduction in PNCO is governed by a defect-mediated hydration mechanism [57,58]:

$$H_2O(g) + V_o^{\cdot\cdot} + O_o^x \rightarrow 2O\dot{H}_o$$

where hydroxyl defects ($OH_o^{\cdot}$) act as mobile proton carriers via a Grotthuss-type hopping mechanism. These protonic defects actively participate in the ORR through a proton-assisted pathway, which proceeds as follows.

1. Oxygen adsorption
$$O_2(g) \rightarrow O_2(ads)$$
2. Proton–electron transfer (formation of hydroperoxide intermediate)
$$O_2(ads) + O\dot{H}_o + e^- \rightarrow OO\dot{H}_o$$
3. Further reduction and protonation
$$OO\dot{H}_o + O\dot{H}_o + e^- \rightarrow 2\dot{O}_o + H_2O(g)$$
4. Reduction to lattice oxygen
$$O_o^{\cdot} + e^- \rightarrow O_o^x$$
5. Oxygen incorporation and vacancy annihilation (overall)
$$\frac{1}{2}O_2(g) + V_o^{\cdot\cdot} + 2e^- \rightarrow O_o^x$$

Therefore, in PNCO, electrons required for oxygen reduction are supplied via small-polaron hopping through mixed-valence Ni^{2+}/Ni^{3+} and Co^{2+}/Co^{3+} redox couples in the classical ORR pathway, whereas under humid conditions, a parallel proton-assisted pathway (Grotthuss-type hopping mechanism) involving hydroperoxide intermediates (OOH) lowers the activation barrier for oxygen reduction. The coupling of electronic conduction, oxygen vacancy transport, and proton mobility significantly enhances surface oxygen exchange kinetics.

3.10 *Electrochemical characterisation of the asymmetric cell*

The electrochemical performance of the fabricated asymmetric cell operating in fuel cell mode with pure hydrogen as the fuel at 800 °C is shown in figure 6a–d. The OCV (1.08 V) suggests a dense electrolyte membrane and good sealing, consistent with the theoretical Nernst voltage of 1.13 V. The V–I graph (figure 6a) shows the cell's reversibility, as evidenced by the symmetry of the curve. The peak current density under dry conditions in the electrolysis mode at 800 °C is 105.11, 81.873, and 53.93 mA cm^{-2} at 1.5, 1.4, and 1.3 V, respectively, as observed from figure 6a. In the presence of humidity, the current density slightly decreases to 93.71, 66.52, and 41.33 mA cm^{-2}. This may be ascribed to water vapor competing with hydrogen for active sites at the fuel electrode. This may lead to site blocking in the perovskite electrode due to increased water partial pressure, which enhances the concentration overpotential, especially in screen-printed layers. This may explain the decrease in current density with humidity, as well documented in the literature [59,60]. Humidity may occasionally accelerate electrode deterioration, leading to reduced electrode activity and, in turn, a decrease in current density [4]. However, according to the literature [2], using a PNCO mesh instead of a screen-printed PNCO oxygen electrode yields current densities of 1720 and 1180 mA cm^{-2} at electrolysis voltages of 1.4 and 1.3 V, respectively, in the presence of humidity. The open 3D mesh architecture provides superior porosity and interconnected channels that facilitate rapid H_2O dissociation, H_2 transport, and water vapor removal from active sites. This eliminates the buildup of concentration overpotential observed in screen-printed layers [2,61].

Also, the Tafel analysis (slope of the I–V curve) of figure 6a shows that the total cell resistance (area-specific resistance (ASR)) is 0.349 Ω cm^2, which is the sum of both the electrolyte resistance and the electrode–electrolyte interfacial polarization resistance. The PNCO-based single cell displays an ohmic resistance of 2.7 Ω cm^2 at 800 °C, which slightly decreases to 2.5 Ω cm^2 in the presence of

Table 4. Comparison of the SOFC button-cell performance in the present study with that of button cells employing different oxygen electrode materials, electrolytes, and operating conditions reported in the literature.

Electrolyte	Oxygen electrode	Operating temperature (°C)	Power density (mW cm^{-2})	Electrolyte Thickness (μm)	Electrode area (cm^2)	Reference
$BaCe_{0.9}Y_{0.1}O_{3-\delta}$	$Nd_2NiO_{4+\delta}$	600	60	27	–	[11]
8YSZ	$SmBa_{0.5}Sr_{0.5}Co_{1.5}Fe_{0.5}O_{5+\ \delta}$	825	32	1090	1	[30]
8YSZ	Pt	400	70.6	0.01	–	[66]
8YSZ	LSM–YSZ	200	78	–	–	[67]
SDCC	–	650	63.3	1000	0.78	[68]
YSZ	LSM	800	1.2	1000	–	[69]
YSZ	$La_{0.595}V_{0.005}\ Sr_{0.4}CoO_{3-\delta}$	800	89	20	0.5	[70]
8YSZ	$PrNi_{0.5}Co_{0.5}O_{3-\delta}$	800	78	818	1	[Present Study]

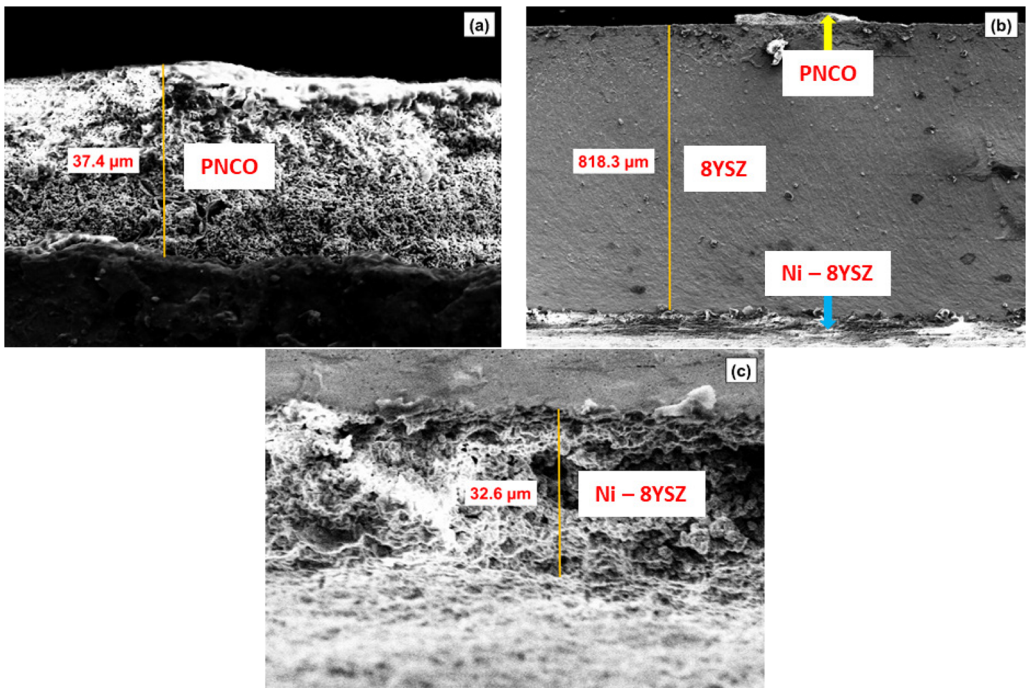

Figure 7. Cross-sectional field-emission scanning electron microscopy (FESEM) images of the tested SOFC after 24 h of operation: (**a**) PNCO oxygen electrode, (**b**) complete cell with 8YSZ as the electrolyte, and (**c**) NiO–8YSZ fuel electrode.

humidity, as shown in figure 6b. The ASR value was directly obtained from the high-frequency intercept of the impedance curve. The ASR in the absence of humidity is 4.73 Ω cm^2, and there is a slight decrease to 4.24 Ω cm^2 in the presence of humidity. The polarization resistance, which indicates the resistance to the charge-transfer reaction at the electrode interface, is obtained from the Nyquist plot by calculating the difference between the real part of the impedance at higher and lower frequencies and is found to be 2.13 Ω cm^2 at 800 °C. This value is slightly reduced to 1.71 Ω cm^2 at 800 °C in the presence of humidity (figure 6b). When humidity is introduced into a triple-conducting oxide material, water molecules dissociate and incorporate into the material's lattice. This creates protonic charge carriers in addition to oxygen ions and electrons, leading to a slight enhancement in conductivity. This may explain the decrease in ohmic resistance in the presence of humidity [62].

From figure 6c, it can be seen that, when using 8YSZ as the electrolyte and comparing the results with the conventional $La_{0.65}Sr_{0.35}MnO_{3-\delta}$ (LSM) electrode and PNCO, the polarization resistance is lower for the cell with PNCO as the oxygen electrode than for the LSM electrode, i.e., 14.06 Ω cm^2 for PNCO and 53 Ω cm^2 for LSM. Hence, a

reduction of almost threefold in the area-specific resistance is observed. The ohmic resistance, which mainly depends on the electrolyte thickness, is 3.25 Ω cm^2. The superior performance of PNCO arises because LSM is primarily a p-type semiconductor with negligible oxide-ion conductivity, which restricts the ORR near the electrolyte interface. In contrast, PNCO enables triple conduction, extending the active reaction zone across the entire cathode thickness [63]. The Ni/Co mixed valence also contributes to this enhanced ORR in PNCO [15,64,65].

From figure 6d, it can be seen that the maximum power obtained at 800 °C for a cell with an 818 μm thick 8YSZ electrolyte and PNCO as the oxygen electrode with an active area of 1 cm^2 is 76 mW cm^{-2}, which is comparatively better than that of a protonic ceramic electrochemical cell with Nd_2NiO_4 as the oxygen electrode, i.e., 60 mW cm^{-2} [11]. A button cell with a thick 8YSZ electrolyte and $SmBa_{0.5}Sr_{0.5}Co_{1.5}Fe_{0.5}O_{5+\delta}$ as the oxygen electrode has reported a power density of 32 mW cm^{-2} at 825 °C [30].

The observed peak power density (~78 mW cm^{-2} at 800 °C) is relatively low compared to optimized SOFCs. However, this is primarily due to the thick YSZ electrolyte (~820 μm), which introduces substantial ohmic resistance, as confirmed by the high-frequency intercept in the impedance spectra. The ohmic resistance scales directly with electrolyte thickness ($R = L/\sigma A$), and the present electrolyte is significantly thicker than those used in practical cells (typically 20–100 μm). Importantly, the impedance analysis shows that the polarization resistance of the PNCO electrode is comparatively low. Furthermore, when benchmarked against a conventional LSM–YSZ cell fabricated under identical conditions, the PNCO electrode exhibits improved electrochemical performance (lower polarization resistance), confirming its superior catalytic activity. The main aim of this work is to evaluate the intrinsic oxygen electrode properties of PNCO. For simplicity and reproducibility, and because the test setup has some limitations for testing thinner cells, a thick electrolyte-supported configuration was employed. Optimization of the cell architecture using thin electrolytes is anticipated to substantially improve the overall performance and will be considered in future work.

As calculated from equation (1), the volume of hydrogen generated from the button cell with a PNCO oxygen electrode, an 8YSZ electrolyte, and a NiO–8YSZ fuel electrode with an active area of 1 cm^2 at 800 °C is 0.732 sccm cm^{-2}. Table 4 presents the SOFC performance of button cells with different oxygen electrode materials, electrolytes, and operating conditions reported in the literature. The results obtained with the present cell are better than those reported in the literature for cells of similar thickness.

3.11 *Microstructure analysis*

The cross-sectional microstructures of the button cell after electrochemical testing are shown in figure 7a–c. The measured thicknesses of the PNCO oxygen electrode, 8YSZ electrolyte, and NiO–8YSZ fuel electrode are approximately 37.4, 818, and 32.6 μm, respectively. Following 12 h of cell operation, the oxygen electrode and the complete cell exhibit microstructural evolution associated with high-temperature exposure, including grain growth and partial sintering. These changes may improve the initial electrode connectivity but can gradually reduce the density of electrochemically active sites during prolonged operation [71].

At the operating temperature (750–800 °C), the NiO–8YSZ fuel electrode undergoes partial reduction of NiO to metallic Ni, accompanied by particle coarsening and neck formation, resulting in a denser microstructure. Such microstructural evolution can alter the triple-phase boundary (TPB) length and influence gas transport within the fuel electrode. Similarly, the PNCO oxygen electrode exhibits a denser morphology with reduced pore volume (figure 7b), consistent with thermally induced sintering during cell operation [72].

The 8YSZ electrolyte remains dense and structurally intact after testing, while the electrode/electrolyte interfaces appear well bonded, with only limited interfacial diffusion expected during operation [73]. Figure 7c reveals localized microcracks and interfacial voids, which are likely associated with thermal stresses arising from the thermal expansion mismatch between the PNCO oxygen electrode and the 8YSZ electrolyte during repeated heating and cooling cycles [73,74]. Localized delamination of the PNCO layer is also observed in some regions of the tested cell. However, some of the observed delamination may have been introduced during specimen sectioning and polishing for microstructural analysis. The relatively higher thermal expansion coefficient (TEC) of PNCO compared with 8YSZ is expected to contribute to interfacial stress development [7]. This mismatch could potentially be mitigated through the use of a suitably matched functional interlayer, and investigations in this direction are currently underway.

Complementary EDS analysis (supplementary table S2) confirms that the principal constituent elements remain confined to their respective layers after 12 h of cell operation, indicating that the overall cell architecture is well preserved. Furthermore, the absence of detectable impurity elements, such as Si or Cr, suggests that neither the fabrication process nor the test environment introduced significant contamination during electrochemical testing.

4. Conclusions

In this study, $PrNi_{0.5}Co_{0.5}O_{3-\delta}$ (PNCO) powder was synthesized using the solution combustion method (SCM). The PNCO powder calcined at 800 °C exhibited a phase-pure orthorhombic perovskite structure with an average agglomerated particle size of 0.2 μm. PNCO pellets sintered

at 1150 °C exhibited a total electrical conductivity of 303 S cm^{-1} at 750 °C, demonstrating their suitability as oxygen electrode materials. Electrolyte-supported button cells were fabricated using NiO–8YSZ as the fuel electrode, 8YSZ as the electrolyte, and PNCO as the oxygen electrode, with both electrodes deposited by screen printing. The electrochemical performance of the electrolyte-supported button cells was evaluated by electrochemical impedance spectroscopy and current–voltage measurements. The cell exhibited a peak power density of 78 mW cm^{-2} at 800 °C.

The oxygen reduction reaction (ORR) in PNCO is proposed to proceed through a synergistic triple-conduction mechanism, in which electrons are transported via adiabatic small-polaron hopping between mixed-valence Ni and Co sites. Under humid conditions, this process is further enhanced by a parallel proton-assisted pathway involving a Grotthuss-type hopping mechanism, which lowers the activation barrier and extends the electrochemically active region. In electrolyzer mode, the button cell produced 0.732 sccm cm^{-2} of H_2 at 800 °C. Reactivity studies of PNCO with the 8YSZ electrolyte indicated slight destabilization of the electrolyte phase. These results suggest that PNCO may not be an ideal oxygen electrode material for use with oxygen-ion-conducting electrolytes such as 8YSZ in fuel cell mode but may be better suited for electrolyzer operation. The relatively low power density, despite the high electrical conductivity of the PNCO electrode, is attributed to poor electrode adhesion. These findings highlight the need to develop suitable interlayers that improve electrode adhesion and accommodate the thermal expansion mismatch between PNCO and 8YSZ.

Acknowledgments

The authors are grateful to Mr. G. Srinivas, Mr. N. Balaji, Mr. Siju, Mr. M. T. Manikandanath, and Ms. S. Latha for their assistance with XRD, particle-size analysis, FESEM, TGA, and XPS measurements, respectively. The authors also sincerely thank Dr. Parthasarathi Bera for assistance with XPS curve fitting. In addition, Ms. Sreelakshmi A acknowledges her colleagues, Pavithra, Mukesh, Darshan, M. S. Sneha, Augustina, Shwetha, Thaniya, and Akhil, for their valuable assistance with the experimental work.

References

[1] Vijaya Lakshmi V, Bauri R, Gandhi A S and Paul S 2011 *Int. J. Hydrogen Energy* **36** 14936
[2] Ding H, Wu W, Jiang C, Ding Y, Bian W, Hu B *et al* 2020 *Nat. Commun.* **11** 1907
[3] Ruiz-Morales J C, Marrero-Lopez D, Canales-Vazquez J and Irvine J T S 2011 *RSC Adv.* **1** 1403
[4] da Conceicao L, Silva A M, Ribeiro N F P and Souza M M V M 2011 *Mater. Res. Bull.* **46** 308
[5] Minh N Q and Mogensen M B 2013 *Electrochem. Soc. Interface* **22** 55
[6] Jadhav L D, Chourashiya M G, Jamale A P, Chavan A U and Patil S P 2010 *J. Alloys Compd.* **506** 739
[7] Sozal M S I, Tang W, Das S, Li W, Durygin A, Drozd V *et al* 2022 *Int. J. Hydrogen Energy* **47** 21817
[8] Laguna-Bercero M A, Kilner J A and Skinner S J 2011 *Solid State Ionics* **192** 501
[9] Choi S, Davenport T C and Haile S M 2019 *Energy Environ. Sci.* **12** 206
[10] Xu X, Wang H, Ma J, Liu W, Wang X, Fronzi M *et al* 2019 *J. Mater. Chem. A* **7** 18792
[11] Dailly J and Marrony M 2013 *J. Power Sources* **240** 323
[12] Yang C, Zhang X, Zhao H, Shen Y, Du Z and Zhang C 2015 *Int. J. Hydrogen Energy* **40** 2800
[13] Sharma R K, Khamidy N I, Rapenne L, Charlot F, Moussaoui H, Laurencin J *et al* 2019 *J. Power Sources* **419** 171
[14] Li Z, Wang J, Zhu J, Sun Y, Wang Z, Zhao Y *et al* 2021 *Sustainable Energy Fuels* **5** 5975
[15] Huang W, Tian C, Meng J, Xu N, Zhang Y, Zhao L *et al* 2024 *J. Phys. Chem. C* **128** 10826
[16] Kerman K, Tallinen T, Ramanathan S and Mahadevan L 2013 *J. Power Sources* **222** 359
[17] Lee S O, Lee D, Jung I, Kim D, Hyun S-H, Kim J *et al* 2013 *Int. J. Hydrogen Energy* **38** 9320
[18] Wolf S E, Vibhu V, Chakraborty P K, Coll C L, Schoner S, Basak S *et al* 2025 *J. Mater. Chem. A* **13** 34565
[19] Deganello F and Tyagi A K 2018 *Prog. Cryst. Growth Charact. Mater.* **64** 23
[20] Jadhav S T, Dubal S U, Jamale A P, Patil S P, Bhosale C H, Puri V R *et al* 2015 *Ionics* **21** 1295
[21] Aruna S T and Mukasyan A S 2008 *Curr. Opin. Solid State Mater. Sci.* **12** 44
[22] Cullity B D 1978 Elements of X-ray Diffraction, 2nd edn. Addison-Wesley Publishing Company, USA
[23] Singh R N, Shivakumara C, Vasanthacharya N Y, Subramanian S, Hegde M S, Rajagopal H *et al* 1998 *J. Solid State Chem.* **137** 19
[24] Sadykov V, Eremeev N, Alikina G, Sadovskaya E, Muzykantov V, Pelipenko V *et al* 2014 *Solid State Ionics* **262** 707
[25] Liu Y L, Hagen A, Barfod R, Chen M, Wang H J, Poulsen F W *et al* 2009 *Solid State Ionics* **180** 1298
[26] Chivite Lacaba M, García Fernandes A, Prado-Gonjal J, Alonso J A, Cascos V 2024 *ACS Appl. Energy Mater.* **7** 8726
[27] Patel B, Inam F, Reece M, Edirisinghe M, Bonfield W, Huang J *et al* 2010 *J. R. Soc. Interface* **7** 1641
[28] Farhad S and Hamdullahpur F 2012 *AIChE J.* **58** 1248
[29] Zheng Y, Shan G E, Zhou X, Chen H, Huang S, Wang S *et al* 2012 *J. Rare Earths* **30** 1240
[30] Packiaraj R, Sreelakshmi A, Ramya J, Kumar S S and Aruna S T 2024 *Mater. Today Commun.* **38** 108355
[31] Pooja and Pawar R, 2026 *React. Chem. Eng.* **11** 49
[32] Fissel A, Dabrowski J and Osten H J 2002 *J. Appl. Phys.* **91** 8986
[33] Lu Q 2024 *ACS Nano* **18** 13973
[34] Yadav P, Sharma A, Goutam U K, Bhaumik I and Sharma G 2024 *J. Alloys Compd.* **1006** 176189

[35] Bagus P S, Nelin C J, Al-Salik Y, Ilton E S and Idriss H 2016 *Surf. Sci.* **643** 142
[36] Suchorski Y, Wrobel R, Becker S, Opalinska A, Narkiewicz U, Podsiadly M *et al* 2008 *Acta Phys. Pol. A* **114** 61
[37] Sanchez-Caballero A, Zamudio-García J *et al* 2025 *ACS Appl. Mater. Interfaces* **17** 21380
[38] Laik B, Richet M, Emery N, Bach S, Perriere L, Cotrebil Y *et al* 2024 *ACS Omega* **9** 40707
[39] Ma Y, Li M, Yan Z, Qiao H, Liu Y, An S *et al* 2025 *ACS Appl. Energy Mater.* **8** 11237
[40] Sun R, Li S, Gao L, An S, Yan Z, Cao H *et al* 2025 *Molecules* **30** 1482
[41] Dillard J G and Koppelman M H 1982 *J. Colloid Interface Sci.* **87** 46
[42] Tabari T, Kobielusz M, Singh D, Yu J and Macyk W 2023 *ACS Appl. Eng. Mater.* **1** 2207
[43] Whitten A, Guo D, Tezel E, Denecke R, Nikolla E and McEwen J-S 2024 *JACS Au* **4** 3104
[44] Wang K, Zhou J, Fu L, Kang Y, Zhou Z, Cheng Y *et al* 2024 *Small* **20** 2404239
[45] Li Z, Mao X, Feng D, Li M, Xu X, Luo Y *et al* 2024 *Nat. Commun.* **15** 9318
[46] Wu M, Yousaf M, Song H, Deng J, Liu Y, Shao J *et al* 2025 *Fuel* **399** 135719
[47] Opitz A K, Nenning A, Rameshan C, Kubicek M, Götsch T, Blume R *et al* 2017 *ACS Appl. Mater. Interfaces* **9** 35847
[48] Li X, He G, Zhou X, Zhang H, Jiang H, Jin Y *et al* 2024 *Mater. Today Energy* **44** 101615
[49] Wang Y, Sui Y, Wang X, Su W, Cao W and Liu X 2010 *ACS Appl. Mater. Interfaces* **2** 2213
[50] Rosten R, Koski M and Koppana E 2006 *J. Undergrad. Mater. Res.* **2** 38
[51] Sadykov V A, Eremeev N F, Vinokurov Z S, Shmakov A N, Kriventsov V V, Lukashevich A I *et al* 2017 *J. Ceram. Sci. Technol.* **8** 129
[52] Yang H, Wang Y, Zhang X, Ma Y and Zhou Q 2025 *Next Mater.* **9** 101161
[53] Lan R, Cowin P I, Sengodan S and Tao S 2016 *Sci. Rep.* **6** 31839
[54] Pagliari M, Marasi M, Montinaro D, Vandoni D, Martelli E, Campanari S *et al* 2025 *J. Power Sources* **649** 237458
[55] Tyunina M, Savinov M, Pacherova O and Dejneka A 2023 *Sci. Rep.* **13** 12493
[56] Mohamed Jibri K P, Archana J, Navaneethan M and Harish S 2023 *Phys. Chem. Chem. Phys.* **25** 12914
[57] Patel S, Liu F, Ding H, Duan C and Ghamarian I 2024 *Int. J. Hydrogen Energy* **72** 1236
[58] Feng P, Yang K, Liu X, Zhang J and Li Z-P 2026 *eScience* **6** 100460
[59] Huang Y L, Pellegrinelli C and Wachsman E D 2016 *J. Electrochem. Soc.* **163** F171
[60] Kamlungsua K and Su P-C 2020 *Electrochim. Acta* **355** 136670
[61] Yang G, Nam S-H, Han G, Fang N X and Lee D 2023 *ACS Appl. Mater. Interfaces* **15** 50427
[62] Zhang W, Zhang X, Song Y and Wang G 2024 *Next Sustain.* **3** 100028
[63] Baek J D, Liu K Y and Su P C 2017 *J. Mater. Chem. A* **5** 18414
[64] Tiwari P and Basu S 2014 *J. Solid State Electrochem.* **18** 805
[65] Ali S A M, Muchtar A, Sulong A B, Muhamad N and Majlan E H 2013 *Ceram. Int.* **39** 5813
[66] Rotureau D, Viricelle J P, Pijolat C, Caillol N and Pijolat M 2005 *J. Eur. Ceram. Soc.* **25** 2633
[67] Kisa A E and Demircan O 2024 *J. Solid State Electrochem.* **28** 1785
[68] Wang N, Tang C, Du L, Zhu R, Xing L, Song Z *et al* 2022 *Adv. Energy Mater.* **12** 2201882
[69] Tong H, Hu W, Fu M, Yang C and Tao Z 2023 *Adv. Sci.* **10** 2304555
[70] Amaya-Duenas D M, Riegraf M, Nenning A, Opitz A K, Costa R and Friedrich K A 2022 *ACS Appl. Energy Mater.* **5** 8143
[71] Laurencin J, Quey R, Delette G, Suhonen H, Cloetens P and Bleuet P 2012 *J. Power Sources* **198** 182
[72] Tarutin A P, Kasyanova A V, Vdovin G K, Lyagaeva J G and Medvedev D A 2022 *Materials* **15** 2166
[73] Elmutasim O, Dhawale D S, Pinczes M, Hamid L, Wong S, Giddey S *et al* 2025 *ACS Appl. Mater. Interfaces* **17** 65225
[74] Delale F and Boduroglu H 1991 *Eng. Fract. Mech.* **39** 45